NUMERICAL AND EXPERIMENTAL INVESTIGATION OF THE AERODYNAMICS OF AN UNCONVENTIONAL W-LEADING EDGE REVERSED DELTA WING IN GROUND EFFECT

M. Musaj*, S. A. Prince*
* City University, London, UK

Abstract

The ground-effect analysis of a W-shaped leading edge, reversed delta planform wing, were carried out by numerical and experimental methods. Results show an increase of the lift and hence lift-to-drag ratio with decreasing ground clearance. Lift-to-drag ratios of 30 are observed for h/b=0.09, which double the values of those for the ground-free case. No major difference in the drag coefficients is noted as the ground is approached. Near-wake plots revealed vortical flow features emanating from the wing which increase in strength in the presence of the ground. Flow separation is more pronounced with decreasing ground clearance. Outward tip vortex movements are also observed with the decreasing ground height, demonstrating an increasing the effective wing aspect ratio.

1 Introduction

This study is part of ongoing research on the aerodynamics of unconventional wing concepts designed to achieve improved performance such as increased lift-to-drag (L/D) ratio, improved stall capability, and enhanced Short Take-Off and Landing (STOL) potential. The current study examines the aerodynamic performance of an unconventional W-shaped leading edge, reversed delta planform wing, (hereafter referred to as the W- wing) in ground effect. The wing, which is based on the AVCEN Jetpod air-taxi wing, features combined backward-forward leading edge sweep and is believed to provide the beneficial qualities of both sweep options in a single design. The effect of aft-sweep on the flight characteristics of aircraft wings has long been recognized. Swept wings are widely employed because of the desire to increase the cruise Mach number and reduce transonic drag [1, 2]. However, with the increase in cruise speed, aircraft wings began to experience the effects of local shock waves. Also, the change in the spanwise distribution of induced angle for the aft-swept wing causes the lift distribution to move outward. Thus, there are limitations of the maximum lift capabilities associated with aft-sweep wing due to early tip stall. The use of forward sweep on the other hand can provide several advantages, such as increased leading edge suction and "soft" stall. Subsonic experimental investigations [3] of forward swept wings have also shown an induced drag reduction, and a higher lift-to-drag ratio [4, 5].

The benefits of the combination of both forward and aft leading edge sweep in a single design have been recognized before. In 1946, Lemme [6], examined the performance of an M-wing, and concluded that in comparison with the aft-swept wing, the M-wing has advantages with regards to propulsion integration and favorable moment characteristics - with increasing angle of attack it became nose heavy instead of tail heavy. Similar combined sweep wing designs have been studied previously by Whitworth, Vickers and Bristol [7]. These designs were intended for supersonic flight, but the high juncture drag associated with combined sweep wings caused the projects to be shelved before any low-speed work had been done. To the author's knowledge there are no investigations on the behavior of the combined sweep wings in ground-effect.

More recently, a combined sweep wing was employed in the concept design of an AVCEN Jetpod air-taxi aircraft. This type of aircraft is typically required to take-off and land

within a distance of 125m. The wing investigated for this study is of the AVCEN planform type, having a NACA 2412 section throughout, with no twist, and comprises of three segments (Fig. 1). It is believed that the properties of this type of wing make it suitable to the performance requirements of such STOL type aircraft. Further, information on the numerical and experimental investigations of the cruise performance of the W-wing is available [8].

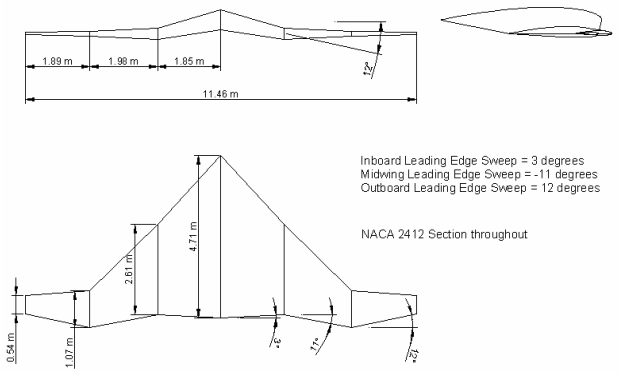

Fig 1. Wing specification

This study is dedicated to assessing the aerodynamic performance capabilities of the W-wing in ground vicinity. It is well acknowledged that take-off and landing are the most dangerous stages of aircraft flight, as the speeds are low and high angles of attack are required. In ground effect, the body tends to "float" and this effect occurs because of the "cushion" of higher pressure air which develops in the cavity between the vehicle and the ground. Extensive research over the years [9,10,11] has shown that the general effect of ground proximity on a wing is a relative reduction of drag, particularly induced drag and evidently an increase of lift-to-drag ratio, as well as increased leading-edge suction giving an increase in the nose-down pitching moment.

Other studies have found conflicting behavior on the subject, where indications of no drag reduction in ground–effect have been reported. Others detail that an increase in lift and drag is noted when the wing is under the ground influence. It has also been reported that flow separation phenomena is increased with ground proximity. Therefore, some of the above mentioned enhanced features would aid further the take-off and landing capabilities which would assist in reducing the required runway length and aircraft clearance, which a very important effect for the STOL type aircraft. Consequently, it is of paramount interest to examine the extent of the increased aerodynamic capabilities of the W-wing, if any, in the influence of the ground. This has been conducted in this study by coupled experimentation and computational analysis. As far as accounting for the ground is concerned, the most successful analytical method is that of Wieselsberger [12]. This theory uses the principle of reflection, where the image of the wing is placed below a ground plane. In this manner the wing will be affected by its image (Fig 2). Experimental methods, on the other hand, range from the fixed ground board to the moving-belt method where the ground boundary layer is removed. The fixed ground method is the least complex method, and although it has some shortcomings, such as boundary layer effects, the method has been proven to be satisfactory provided it is not employed with very low ground clearences. Wieselsberger's image method was used for the numerical simulations of this study, whereas a static ground board was used for the experimental investigations.

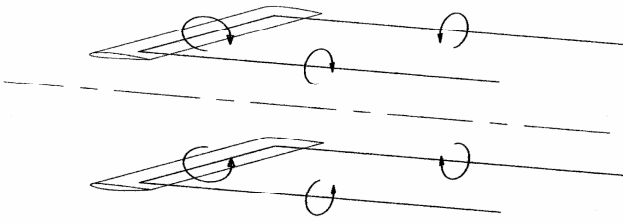

Fig 2. Horseshoe Vortex Distribution in Ground Effect

The following outlines the experimental and numerical results obtained on the scale model of the isolated wing in ground-effect. Additionally, numerical analyses of the full-scale wing are also included. Further analyses were carried out to assess the behavior of some of the previously noted stalled flow features in the presence of ground proximity.

2 Experimental Arrangements

The T3 tunnel was employed for the experimental investigations of this study. The tunnel is a low speed, closed-circuit return type wind tunnel, with a regular octagonal working section of maximum width 115 cm, height 89 cm and length 150 cm, (see Fig 3). The tunnel is fitted with a three-component balance system, externally positioned above the working section, and has a motorized pitch mechanism for controlling incidence. T3 employs an inverter that is capable of continuous variation of velocity in the range of approximately 3 m/s up to 45 m/s. Wind speed is measured by a Furness FCO16 digital water manometer, which indicates the difference between the tunnel working section and contraction pressures.

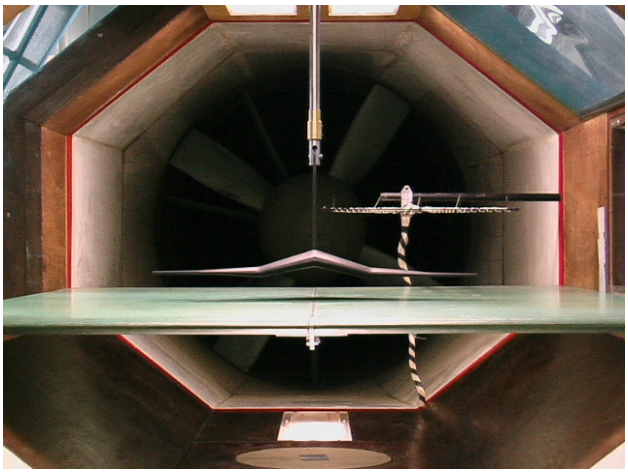

Fig 3. Downstream view of the mounted wing with ground board and wake rake.

After passing the contraction section the free-stream longitudinal turbulence intensity in the empty working section is known to be around 0.5%. Previous tests in T3 have shown the velocity distribution to be fairly uniform with the variation across the majority of the working section being confined to less than 1.5%.

2.1.2 Wing Model

A 5% scale model of the AVCEN Jet-pod wing was built in the Centre for Aeronautics workshop, the size of which was chosen to be based on a maximum 60cm full span. This decision was influenced by the size of the tunnel working section, and the desire to keep blockage low, whilst providing the greatest Reynolds number possible. Due to the nature of the T3 tests the balance pitch mechanism could not be employed. Therefore, the angle of attack had to be varied manually during the run. A systematic approach to changing the angle of attack was adopted before each run, where the wing angle of attack was initially set at 0º, as measured by a FISCO Solatronic Inclinometer which has an accuracy of ±0.2º.

2.1.3 Ground Board

Although experimental methods to assess ground effect generally require complex systems to ensure accurate ground simulation, a simplified approach that uses a fixed board, typically adopted to reduce time and cost (as is the case here), may be employed with reasonable results, as long as extremely low ground clearances are avoided [13,14].

The ground board used for the current study was a straight-walled wooden plane of constant thickness. The board was 1385 mm long, 1146 mm wide (spanning the width of the tunnel), and had a thickness of 225 mm (see Fig. 4). The leading edge was elliptical, with a 3:1 ratio. The wing was the positioned at various ground clearances relative to the board, measured as height-to-span ratios (*h/b*).

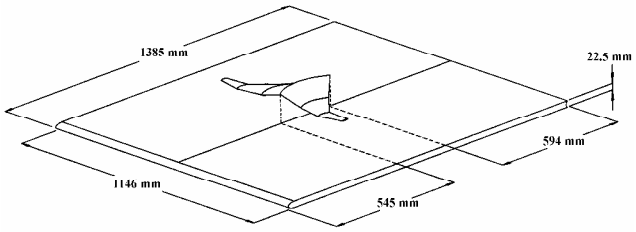

Fig 4. Schematic of the Wing Model Set-up with Respect to the Ground Board

Prior to testing, an effort was undertaken to characterise the flow in the empty tunnel environment. As part of this effort, a rake system was employed to measure the boundary layer of the ground plane at both the location where the model was to be mounted and downstream of the model where near-wake investigation would take place. In these flow

conditions, the measured velocity profile indicated that the edge of the boundary layer (u/U~0.99) occurs at a height of approximately 15 mm from the ground board. In order to validate some of the near-wake phenomena noticed in the numerical analysis, sets of tests were carried out to examine the near-wake behind the model. This involved the measurements of dynamic pressure distribution using a horizontally positioned wake rake, as depicted in Fig. 5.

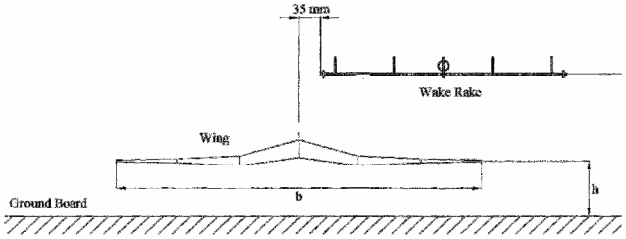

Fig 5. Wake Rake Positioning

The rake consists of forty pitot tubes and five static tubes. Static tubes are positioned parallel to the pitot rake except offset by 25 mm, to avoid interference effects on the static pressures. Rake pressure data were taken x/c_r=1.5 measured from the root trailing edge.

3 Numerical Methods

For the numerical analysis the incompressible Navier-Stokes equations were solved. The equations were expressed in conservation form as follows:

$$\frac{\partial}{\partial t}\int W dV + \oint [F - G] dv = \int_V H dV \tag{1}$$

The vector of the dependant variables W and the flux vectors F, G, and H are given as

$$W = \begin{bmatrix} \rho \\ \rho v \\ \rho E \end{bmatrix}, F = \begin{bmatrix} \rho v \\ \rho v \times v + pI \\ \rho v H + pv \end{bmatrix} \tag{2}$$

$$G = \begin{bmatrix} 0 \\ T \\ Tu + q^{"} \end{bmatrix}, H = \begin{bmatrix} 0 \\ f_r + f_g + f_p + f_u \\ 0 \end{bmatrix} \tag{3}$$

The viscous fluxes are written in stress tensor form. For turbulent flow they are as follows:

$$T = T_l + T_t$$
$$T_t = \mu_{eff}\left[\nabla v + \nabla v^T - \frac{2}{3}(\nabla \cdot v) I\right] \tag{4}$$

The laminar viscosity was determined via Sutherland's Law:

$$\frac{\mu}{\mu_0} = \frac{(T_0 + S)}{(T + S)}\left(\frac{T}{T_0}\right)^{\frac{3}{2}} \tag{5}$$

where S = 111K is Sutherland's constant.

Equation (1) was discretized using a finite volume technique, and the solution of the governing equations was obtained using the STARCCM+ cell-based, hybrid unstructured mesh Navier-Stokes flow solver. The solver was validated against experimental data available for the Onera M6 wing [15], and very good agreement was achieved.

Segregated quasi-steady incompressible solutions were obtained for the wind tunnel model simulations, as well as for the full-scale conditions. The solver also employs a preconditioning matrix, which is necessary for lower Mach number flows. For the current study, Menter's k-ω Shear Stress Transport (SST) turbulence model [17] (with suitable wall functions) was used, since this model was found to agree better with experiments on the M6 and the current wing [8].

Only half of the wing was modeled, with symmetry boundary conditions being used to simulate the full configuration. The far-field boundaries were extended to about ten root-chord lengths from the wing surface geometry in the upstream, radial, and downstream directions. The ground was simulated with the symmetry plane boundary conditions. The computational model for the wind tunnel simulations did not include any mounting hardware or wind tunnel structure, as the wind tunnel data were corrected for blockage and tare effects. Unstructured viscous computational grids were used to discretize the domain.

4 Results of Experimental and Numerical Analyses

Initially for the experimental tests, various velocities were tested to assess the Reynolds number effects, if any, on the lift, drag and pitching moment behavior of the wing. As no

major difference in the force coefficient results were observed as the Reynolds number was varied a final choice of 30 m/s as the most convenient velocity was made. The experimental tests were therefore run at a Reynolds number of $Re=3x10^5$ and Mach number of 0.09. Testing covered a range of angles of attack ($-10^o<\alpha<30^o$), with steps of approximately $\Delta\alpha=2^o$, and ground clearances ($0.045<h/b<0.55$).

Numerical simulations were carried out at the same conditions as the experimental tests ($Re=3x10^5$ and $M=0.09$, $0.09<h/b<0.55$). To provide a comparison with the image (symmetry) method, simulations with a fixed ground plane were also carried out.

Because of the "symmetry plane" ground simulation strategy employed in this study, separate grids had to be generated for each combination of angle of attack and *h/b* ratio considered. Due to the unstructured nature of the grid, no grid was of the exact same number of cells as any other; however, a range of approximately 2.6 to 2.8 million hybrid tetra/prism/pyramid cells was maintained A total of 20 to 22 prism layers were implemented to account for the wing's boundary layer.

Along with the momentum residuals, force and moment coefficients were observed as a convergence criterion for the numerical tests. The solutions were considered to have converged when no variations greater than ±0.001 in either the force (C_L and C_D) or moment coefficients were observed over 100 iterations. The level of convergence and the residual order of magnitude were both distinctly enhanced as the wing moved further away from the ground.

Fig 6 and 7 represent the longitudinal aerodynamic characteristics (lift, drag coefficients) of the W-wing, as obtained by experimental and Navier-Stokes computations. The mechanism implemented to alter angle of attack interfered with the ability to accurately measure the pitching moment, hence no comparison between experimental and numerical moment data was possible. The choice of the pitching mechanism was unavoidable; however, in comparison with previous tests it improved the near-wake flow quality.

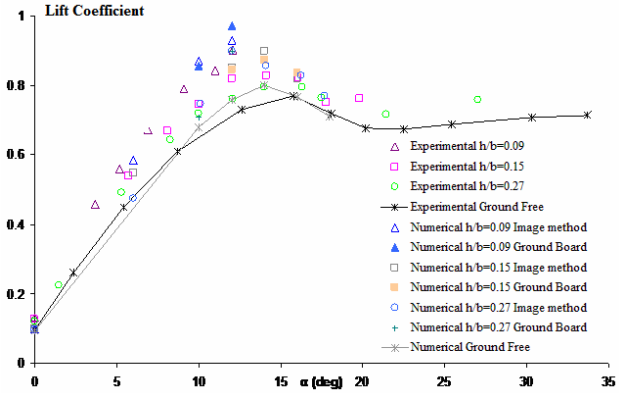

Fig 6. Numerical and Experimental variation of lift coefficient with angle of attack at various h/b

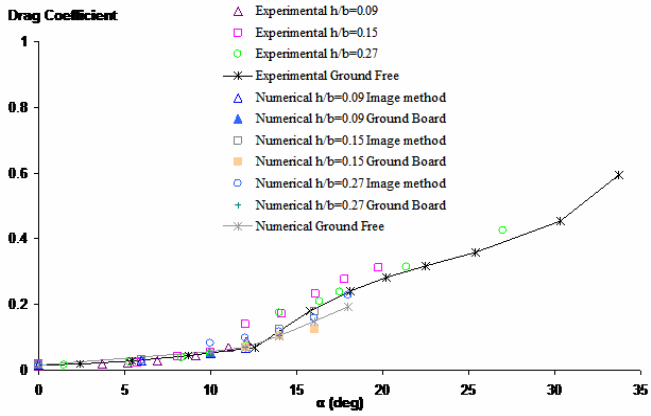

Fig 7. Numerical and experimental variation of lift coefficient with angle of attack at various h/b

The results show a slight disagreement between experiment and CFD on the lift coefficient results, which increases with increasing angle of attack. It can be observed that the greatest difference between the numerical results obtained by the image method and the experimental data is present at maximum lift conditions. The difference between the two investigations is also noticed to increase with increasing ground clearance. The best agreement between the two methods was observed at *h/b*=0.09, with the image method giving slightly higher lift coefficient values at the highest angle investigated ($\alpha=12^o$). At this angle the numerical simulation with the ground board present gave a better agreement with the experimental results. This result was noted for all the cases investigated, where the fixed

ground board numerical simulations always gave a better agreement with the experimental results. These findings are in agreement with previous studies, where the image method was found to give higher lift when compared to the static wind tunnel test results [18]. On the other hand, surprisingly excellent agreement is achieved between the experimentally and numerically derived drag results, especially at the lower angles of attack. Both the image and the fixed ground numerical simulations give very similar results, which are almost identical to the experimental data. Minor disagreements are mostly noticeable at the higher angle of attack range, where the drag coefficients for *h/b*=0.15 are smaller when obtained by numerical simulation. It was also observed that for angles higher than α =12º and *h/b* below 0.27, an increase in drag is apparent.

From both lift and drag coefficient plots it can be seen that the effect of the ground starts to deteriorate at *h/b*=0.45, above which the coefficients are almost identical to those from the ground free case. In the experimental investigations, ground height ratios of *h/b*>0.45 were not achievable due to the wind tunnel working section and support system limitations

The effect of the ground is observed to occur even at α=0º, which is contrary to the general trend. Unlike other studies [9,10,11,19], no major difference was noted from the drag coefficient plots for all *h/b* ratios investigated, especially at lower angles of attack.

From the above findings it also needs to be noted that the effect of the fixed-ground boundary layer is more prominent as α increases, which is also noticed here. The disagreement, therefore, is attributable to the shortcomings of the experimental method employed as well as the limited number of sensitivity analyses, which was influenced by the amount of grids required for this study.

4.2.1 Results Real-flight Numerical Analyses

Full-scale numerical simulations were run at Reynolds number of 6.9 x10^6, Mach number of M=0.11 and 0.045<*h/b*<0.55. Fig. 8 to 11 present the lift, drag and pitching moment coefficients as well as the lift-to-drag ratio and C_D-C_{D0} (where C_{D0} is the drag at zero angle of attack). As it can be observed, the lift coefficient increases with decreasing ground clearence, reaching a C_L of 1.2 at *h/b*=0.09 and α=12º - an increase of approximately 33% in comparison with out of ground data.

From the drag coefficient data (Fig. 9), barely any change of the drag can be seen with varying ground clearence. Only a minor decrease is noticed at the higher angles of attack, whereas at the lower angles the data matches the out of ground effect results. Previous studies, suggested a greater decrease in induced drag with the influence of the ground. To carry out a comparison, plots of C_D-C_{D0} were generated and are shown in Fig. 11. From these plots it can be seen that in fact a minor decrease in the induced drag is indeed present, as the value of C_D-C_{D0} decreases as the wing approached the ground.

Lift-to-drag plots reveal a great increase with ground proximity where ratios of as high as 30 are noted from the full-scale simulations. These values are almost double that of the ground-free case (L/D=16). This is a significant increase in comparison with other studies of conventional wings. The L/D then decreases with the increasing ground height, giving 33% increase at *h/b*=0.145 and 20% increase at *h/b*=0.145.

It was observed that at *h/b*=0.55 the wing seems to be out of the influence of the ground at the lower angles of attack; however, ground influence is still apparent at higher angles of attack.

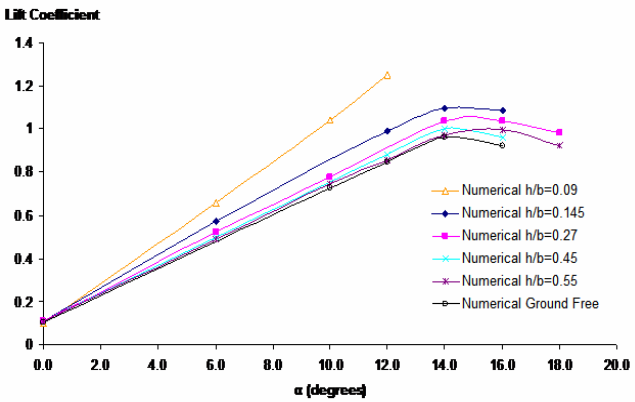

Fig 8. Full-scale numerical variation of lift coefficient with angle of attack at various h/b

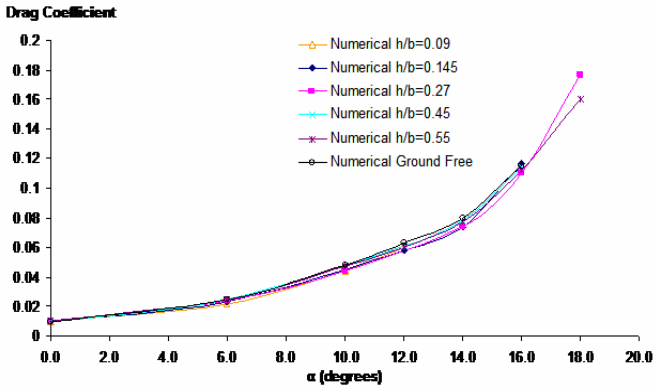

Fig 9. Full-scale numerical variation of drag coefficient with angle of attack at various h/b

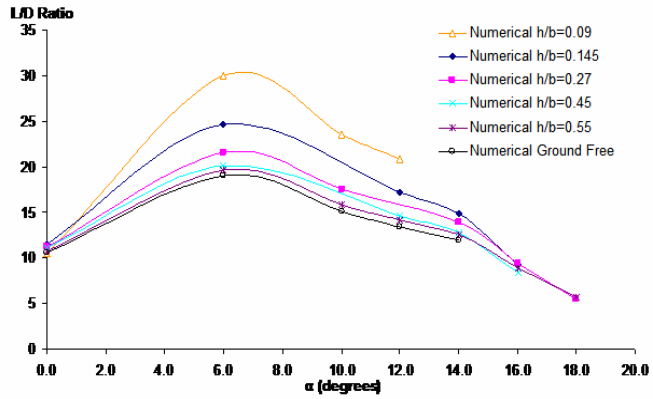

Fig 10. Full-scale numerical variation of L/D ratio with angle of attack at various h/b

Pressure distributions are also discussed below, to further examine the behavior of the W-wing in ground proximity.

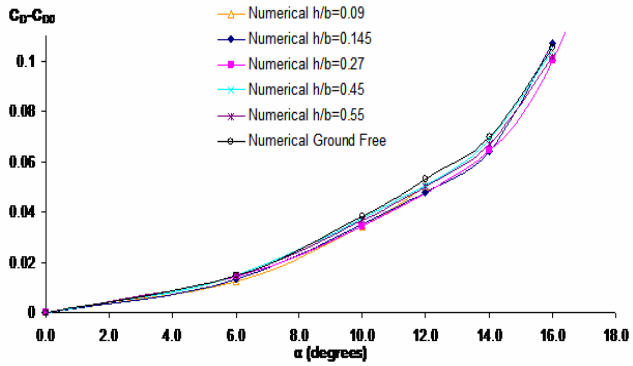

Fig 11. Full-scale numerical variation of C_D-C_{D0} with angle of attack at various h/b

Fig 12. presents the upper and lower surface pressure distribution for the ground-free case at a Reynolds number of 6.9×10^6 and Mach number, M=0.11. Fig. 13 illustrates the pressure distribution at the same flow conditions as above and *h/b*=0.09. As expected lower surface pressures increase with decreasing ground clearance, particularly near the wing leading edge. Similarly, an increase is noticed with increasing angle of attack, with regions of high pressure covering a large part of the lower wing. This was furthermore apparent at *h/b*=0.145 (Fig. 14), where the wing is clearly still under ground influence. Results also showed that ground effect increases slightly the magnitude of the leading edge suction region on the upper surface of the wing.

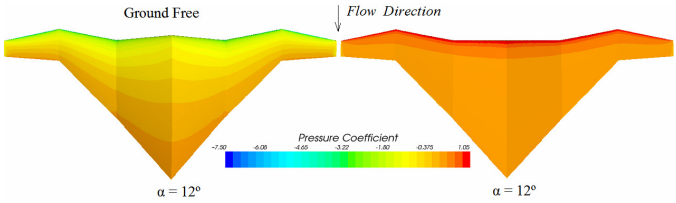

Fig 12. Predicted pressure distributions on the upper and lower surfaces at ground free

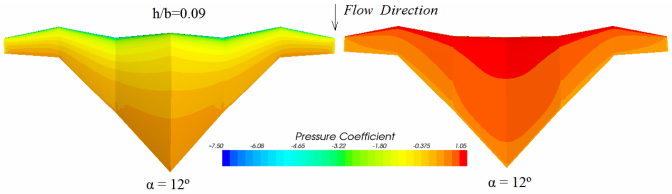

Fig 13. Predicted pressure distributions on the upper and lower surfaces at h/b=0.09

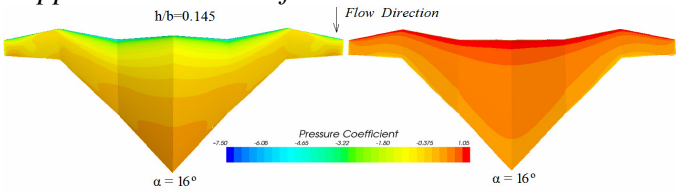

Fig 14. Predicted pressure distributions on the upper and lower surfaces at h/b=0.145

For the purposes of detailing the effect the wing on the ground, mach contours on the symmetry plane are plotted. It can be observed that for small clearances (h/b=0.09) regions of very slow moving flow are observed underneath the wing, and the symmetry plane at these settings is subjected to very strong pressure variations. The air tends to stagnate under the wing which results in the high pressures of the so-called "air cushion" effect of the wing in

ground effect [20]. It can also be seen that at the symmetry plane underneath the mid part of the wing span, regions of very high velocity are noticed. The W-wing at low ground clearances creates a rather strong such effect, which is advantageous when short-take-off requirements are to be met. As the wing moves further from the ground (fig 16) its influence on the ground is reduced and therefore the ram-effect is noticed to diminish.

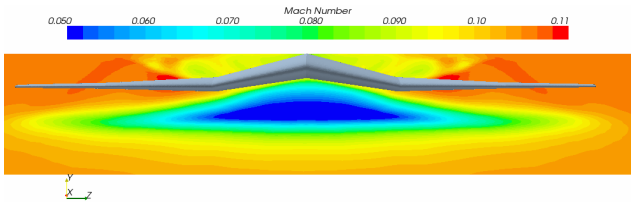

Fig 15. Ground Mach distribution contours at h/b=0.09 and α=12º

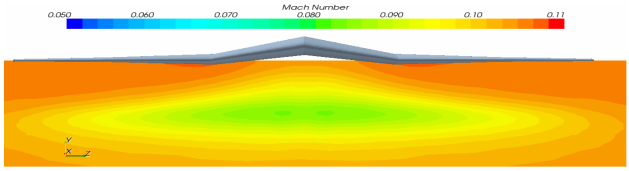

Fig 16. Ground Mach distribution contours at h/b=0.145 and α=12º

Furthermore, plots of surface shear stress / friction lines are presented to highlight the effect of the ground on the flow separation at the sensitive near-stall angles. Fig. 17 shows the surface friction lines at *h/b* =0.09 and *h/b*=0.45 at α=12º. It can be seen that in the presence of the ground the spanwise flow is more pronounced, as the friction lines show a more severe mid-wing spanwise flow. The surface friction lines are closer to each other and the shear-stress magnitude is reduced. Therefore, greater regions of almost zero shear-stress magnitude are observed for this case, suggesting an increased tendency for the onset of trailing edge separation when compared to *h/b*=0.45, where the wing is further away from the influence of the ground. At stall, (i.e. α = 16º) as noted in fig 18 the flow has separated from the tip. The flow at *h/b*=0.145 is separated over a greater part of the wing when compared to *h/b*=0.27 case. These figures show that the ground does in fact affect the spanwise movement and separation onset, with increasing severity as the wing approaches the ground. It also needs to be mentioned that, at the current flow conditions, the leading-edge inboard crank does not seem to effect in the flow separation, as in high-speed cases [8].

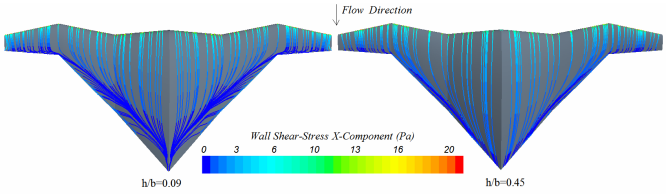

Fig 17. Wall shear-stress streamline distribution for h/b=0.09 (left) and h/b=0.145 (right) at α= 0º

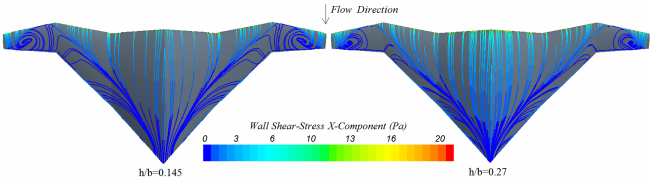

Fig 18. Wall shear-stress streamline distribution for h/b=0.145 (left) and h/b=0.27 (right) at α=16º

4.2.2 Near-wake experimental and numerical results

Previous studies on the W-wing at free-flight conditions reported that a vortical stall cell feature was noticed to emanate from mid-wing at stall conditions [8]. This was observed from near-wake analyses of both low-speed wind tunnel tests on the scaled wing and full-scale numerical simulations. This study focused on the wing near-wake when in ground proximity. Total pressure measurements are taken at the downstream location of x/c_r=1.5. Similarly with the force coefficient plots, near-wake experimental investigations were carried out for various ground clearences.

Fig 19 illustrates the near-wake behavior for *h/b*=0.045 and *h/b*=0.06, at α=0º. From these plots it can be seen that at α=0º for *h/b*=0.045, the wake of the wing is completely merged with the ground boundary layer, with a noticeably larger wake at the mid-wing when compared with the ground-free case [8]. Similarly, at α=0º

and *h/b*=0.045 the wing mid- and outer-section wake is not present in the plots which suggests interference with the ground boundary layer. A vortical roll-up underneath the tip is noticed at both these very low ground heights. This ground vortex seems to be induced by the tip vortex which causes the ground boundary layer to separate. The near-wake performance at these ground heights is not comparable with the ground-free case as the severe interference from the ground boundary layer is not present in real flight with low atmospheric wind.

The strength of the vertical features in the wake are seen to be enhanced (see Fig 20) in the presence of the ground as observed for the *h/b*= 0.09 and α=12°.

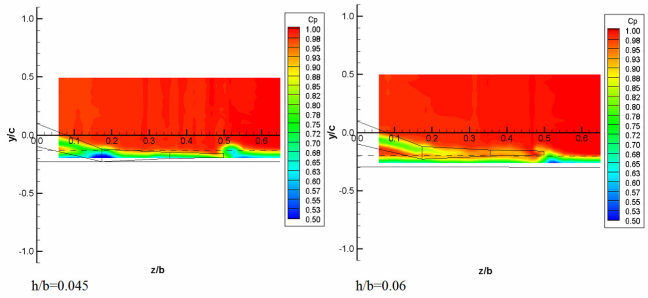

Fig 19. Near-wake total pressure coefficient plot for h/b=0.045 (left) and h/b=0.06 (right) at α= 0°

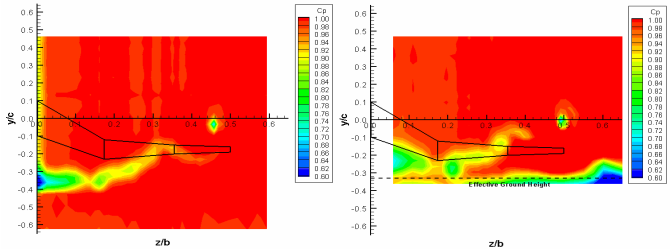

Fig 20. Near-wake total pressure coefficient plot for ground free case (left) and h/b=0.09 (right) at α=12°

An interesting feature which can be observed from these near-wake plots is the outward tip vortex movement, which increases with decreasing ground height. It is known that this movement will increase the effective span and thereby aspect ratio of the wing and therefore the lift and L/D ratio. A top-view of the tip vortex movement from the numerical simulations of three ground heights (*h/b*=0.09, *h/b*=0.145) is shown in Fig 21. It can be seen that in ground effect (i.e *h/b*=0.09), at a given downstream location, the tip vortex moves outboard by almost the same distance as the inboard tip vortex shift when out of ground (i.e *h/b*=0.45). This outboard movement of the vortex cores suggests that their influence on the wing and on any tail surface would be reduced [20].

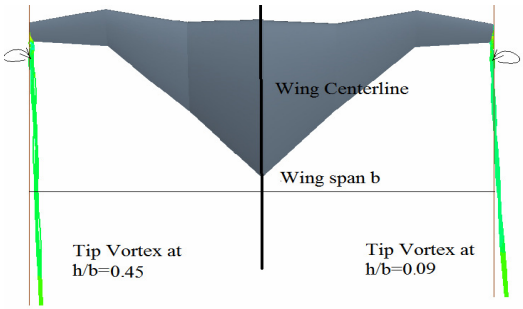

Fig 21. Outward tip vortex movement

Off-surface streamlines are plotted in figure 22. Interestingly the off-surface streamlines, complemented by the near-wake behaviour, provide an explanation of the previously noticed high-velocity flow on the symmetry plane Mach contours. The results show clearly by comparing the figures for *h/b*=0.09 and *h/b*=0.45, both at α =12°, that the reason behind the high velocity outboard flows is the interaction of the wake with the symmetry/ground plane (fig 22). The plots reveal a strong interference of the symmetry/ground with the wing wake.

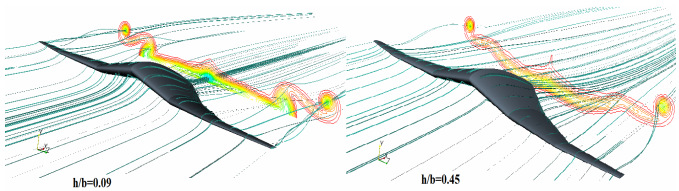

Fig 22. Off-surface streamlines and near-wake at h/b=0.09 and h/b=0.45 and α=12°

5 Conclusions

The results show a great increase of the lift coefficient and lift-to-drag ratio for the W-wing in ground effect. Values of L/D=30 are achieved for h/b=0.09, which doubles the L/D in free-flight. Regions of very low velocity and high pressure underneath the wing have been resolved, suggesting a very strong “air cushion”

effect being induced by the wing. The high L/D ratios for the W-leading edge, reversed delta wing planform were found to be particularly high when compared with similar data for simple planar wings. Such high L/D ratios are very desirable for the performance of the STOL type aircraft for which the wing is intended. Furthermore, the spanwise flow velocties over the upper surface are increased with the decreasing ground height and the associated stall vortex features are strengthened for cases of the higher angles of attack.

6 References

[1] Jones, R. T. Wing Plan Forms for High-Speed Flight. NACA Report 863, 1947

[2] Furlong GC. and McHugh GJ. A Summary and Analysis of the Low-Speed Longitudinal Characteristics of Swept Wings at High Reynolds Numbers. NACA Report 1339, 1952.

[3] Boucheron O and Brocard Y, Comparison of Aerodynamic Characteristics of Aircraft with Forward and Aft Swept Wings at Mach 0.5. ONERA.

[4] Forward Swept Wing Potential Studied. *Aviation Week and Space Technology*, Vol. 110, No.5, pp. 126-127.1979.

[5] Spacht G. The Forward Swept Wing: A Unique Design Challenge. *Proceedings of the AIAA Aircraft Systems Meeting*, Anaheim, CA, 1980.

[6] Lemme HG. Investigation on a Normal Swept-Back Wing, a Blunted Swept Back Wing and an M Wing. British M.O.S (a),Volkenrode, Reports and Translations No. 441, 1946.

[7] Payne R. *Stuck on the Drawing Board: Un-built British Commercial Aircraft since 1945*, Tempus Publishing, Ltd., Gloucestershire, UK, 2005.

[8] Musaj M. et al (2008) Computational and Experimental Investigation of the Aerodynamics of Unconventional W Wings. *46th AIAA Aerospace Sciences and Meeting Exhibit*, Reno, NV, AIAA-2008-0415.

[9] Suh YB and Ostowari C. Drag Reduction Factor Due to Ground Effect. *Journal of Aircraft* Vol 25, No.11, pp 1071-1073,1988.

[10] Tuck K. Nonlinear extreme Ground Effects on Thin Wings of Arbitrary Aspect Ratio. *Journal of Fluid Mechanics.* Vol 136, pp 73-84. 1983.

[11] Morishita E and Tezuka K. Ground Effect Calculation of Two-Dimensional Airfoil .*Trans. Japan Soc. Aero. Space Sci*. Vol 36, No. 114,pp 270-280. 1994

[12] Wieselsberger C. Wing Resistance Near the Ground. ACA TM 77. 1922.

[13] Lockwood V E. and Phillips WP. Measurents of Ground Effect on a Low-Apect -Ratio Ogee-Wing Airplane Model and Calculations of Landing-Flare Trajectories. NASA TN D- 4329.1968.

[14] Thomas J L et al. Powered Low-Aspect -Ratio Wing in Ground Effect (WIG) Aerodynamic Characteristics. NACA TM-78793. 1979

[15] Schmitt V and Charpin F. Pressure Distribution on the Onera M6 Wing at Transonic Mach Numbers. AGARD-AR-138. 1979.

[16] Menter F. Two-Equation Eddy-Viscosity Turbulence Modeling for Engineering Applications. *AIAA Journal*, Vol. 32, No. 8, pp. 1598-1605.1984

[17] George A. Aerodynamic Effects of Shape, Camber, Pitch and Ground on Idealized Ground Vehicle Bodies. *Journal of Fluid Mechanics*,Vol,103,pp 631-638.1981

[18] Hsiun CH and Chen CK. Aerodynamic Characteristics of a Two-Dimensional Airfoil with Ground Effect. *Journal of Aircraft* Vol 33, No. 2.1996

[19] Staufenbiel RW and Schlichting UJ. Stability of Airplanes in Ground Effect. *Journal of Aircraft.* Vol 25. No.4. pp 289-294. 1998

[20] Baker MD et al. Numerical Investigation of Slat and Compressibility Effects for a High-Lift Wing. *Journal of Aircraft*. Vol 39. No.5.pp 876-884.2002

Copyright Statement